This is a preprint, the final version is subject to change, of the American Mineralogist (MSA)
Cite as Authors (Year) Title. American Mineralogist, in press.
(DOI will not work until issue is live.) DOI: http://dx.doi.org/10.2138/am-2017-5907

Co-variability of S^{6+}, S^{4+} and S^{2-} in apatite as a function of oxidation state – implications for a new oxybarometer

Revision #1

Brian A. Konecke[1,*], Adrian Fiege[1,2], Adam C. Simon[1], Fleurice Parat[3], André Stechern[4]

[1]Department of Earth and Environmental Sciences, University of Michigan, Ann Arbor, Michigan 48109, USA.

[2]Department of Earth and Planetary Sciences American Museum of Natural History, New York, New York 10024-5192, USA.

[3]Géosciences Montpellier, Université Montpellier, Place E. Bataillon, 34095 Montpellier, France.

[4]Institut für Mineralogie, Leibniz Universität Hannover, Callinstr. 3, D-30167, Hannover, Germany.

*Corresponding author: bkonecke@umich.edu

ABSTRACT

In this study, we use micro X-ray absorption near-edge structures (μ-XANES) spectroscopy at the S *K*-edge to investigate the oxidation state of S in natural magmatic-hydrothermal apatite (Durango, Mexico and Mina Carmen, Chile) and experimental apatites crystallized from volatile-saturated lamproitic melts at 1000°C and 300 MPa over a broad range of oxygen fugacities ((log(fO_2) = FMQ, FMQ+1.2, FMQ+3; FMQ = fayalite-magnetite-quartz solid buffer). The data are used to test the hypothesis that S oxidation states other than S^{6+} may substitute into the apatite structure. Peak energies

This is a preprint, the final version is subject to change, of the American Mineralogist (MSA)
Cite as Authors (Year) Title. American Mineralogist, in press.
(DOI will not work until issue is live.) DOI: http://dx.doi.org/10.2138/am-2017-5907

corresponding to sulfate S^{6+} (~2482 eV), sulfite S^{4+} (~2478 eV) and sulfide S^{2-} (~2470 eV) were observed in apatite, and the integrated areas of the different sulfur peaks correspond to changes in fO_2 and bulk S content. Here, multiple tests confirmed that the S oxidation state in apatite remains constant when exposed to the synchrotron beam, at least for up to 1-hour exposure (i.e., no irradiation damages). To our knowledge, this observation makes apatite the first mineral to incorporate reduced (S^{2-}), intermediate (S^{4+}), and oxidized (S^{6+}) S in variable proportions as a function of the prevailing fO_2 of the system.

Apatites crystallized under oxidizing conditions (FMQ+1.2 and FMQ+3), where the S^{6+}/S_{Total} peak area ratio in the co-existing glass (i.e., quenched melt) is ~1, are dominated by S^{6+} with a small contribution of S^{4+}, whereas apatites crystallizing at reduced conditions (FMQ) contain predominantly S^{2-}, lesser amounts of S^{6+}, and possibly traces of S^{4+}. A sulfur oxidation state versus S concentration analytical line transect across hydrothermally altered apatite from the Mina Carmen iron oxide-apatite (IOA) deposit (Chile) demonstrates that apatite can become enriched in S^{4+} relative to S^{6+}, indicating metasomatic overprinting via a SO_2-bearing fluid or vapor phase. This XANES study demonstrates that as the fO_2 increases from FQM to FMQ+1.2 to FMQ+3 the oxidation state of S in igneous apatite changes from S^{2-} dominant to $S^{6+} > S^{4+}$ to $S^{6+} >> S^{4+}$. Furthermore, these results suggest that spectroscopic studies of igneous apatite have potential to trace the oxidation state of S in magmas. The presence of three S oxidations states in apatite may in part explain the non-Henrian partitioning of S between apatite and melt. Our study reveals the potential to use the S signature of apatite to elucidate both oxygen and sulfur fugacity in magmatic and hydrothermal systems.

Keywords: apatite, sulfur oxidation state, XANES, oxybarometer, apatite crystallization experiments

INTRODUCTION

Sulfur is the third most abundant volatile in magmatic systems released during volcanic eruptions and degassing processes (cf. Faure, 1986; Métrich and Mandeville, 2010; Mandeville, 2010) and is the fundamental chemical anomaly in arc-related magmatic-hydrothermal porphyry-type ore deposits, which are an important source of Cu, Au, Ag, and Mo (Gustafson and Hunt, 1974; Candela and Piccoli, 2005). A growing body of data suggests that the oxidation state of S (e.g., S^{2-}, S^{4+}, S^{6+}) plays a fundamental role in controlling ore metal solubilities in parental silicate melts, and partitioning of ore metals between melt and magmatic-hydrothermal ore fluids (Simon and Ripley, 2011). Sulfur oxidation state in silicate melts and magmatic-hydrothermal fluids is intrinsically linked to oxygen fugacity (fO_2), where sulfur is present as sulfate (S^{6+}) and sulfide (S^{2-}) in oxidized and reduced silicate melts, respectively (Jugo et al., 2010). While sulfur in aqueous fluids that exsolved from oxidized and reduced silicate melts exists as sulfite (S^{4+}; SO_2), sulfide (S^{2-}; H_2S; Burgisser et al., 2015) and a trisulfur ion (S_3^-; Pokrovski et al., 2011, 2015).

The mineral apatite—commonly $Ca_5(PO_4)_3(F, Cl, OH)$—is an ubiquitous phase in terrestrial (Webster and Piccoli, 2015) and extraterrestrial (McCubbin and Jones, 2015) magmatic and magmatic-hydrothermal systems and incorporates redox sensitive elements such as Fe, Mn and S. Mainly based on the observation that S-rich (terrestrial) apatite is typically observed in relatively oxidized environments, sulfate (S^{6+}) has been suggested to replace other cations in the apatite structure via several independent substitutions (e.g.,

This is a preprint, the final version is subject to change, of the American Mineralogist (MSA)
Cite as Authors (Year) Title. American Mineralogist, in press.
(DOI will not work until issue is live.) DOI: http://dx.doi.org/10.2138/am-2017-5907

Rouse and Dunn, 1982; Liu and Comodi, 1993; Tepper and Kuehner, 1999; Parat et al., 2011b):

$$P^{5+} + Ca^{2+} = S^{6+} + Na^{+} \quad [1]$$

$$2P^{5+} = S^{6+} + Si^{4+} \quad [2]$$

However, apatite crystallized from reduced (sulfide-only) silicate melts has also been shown to contain relatively significant amounts of S. For example, analysis of lunar apatite from the Apollo 12 (sample 12039,42) and 15 (sample 14053,241) missions revealed relatively high S concentrations of >400 μg/g (Boyce et al., 2010; 2014) under low fO_2 conditions relevant for lunar magmatic systems (e.g., ≤ΔIW+0; Sato et al., 1973), where the $S^{2-}/\Sigma S$ ratio of the system is ~1 (cf. Jugo et al., 2010). Boyce et al. (2010) suggested that the relatively S-rich lunar apatite might indicate the incorporation of S^{2-} into the apatite structure under reducing conditions. If apatite can incorporate S oxidation states other than S^{6+}, and if the S oxidation state and S content in apatite correspond to the S signature of the co-existing melt, then it seems plausible that apatite may reliably record changes in S contents and S speciation during the evolution of magmatic systems. Considering the apatite's ability to crystallize from (silicate) melts and magmatic-hydrothermal fluids (e.g., Lyons, 1988; Peng et al., 1997; Streck and Dilles, 1998; Parat et al., 2004; 2011B; Webster and Piccoli, 2015; Mao et al., 2016), intracrystalline zonation in S content and oxidation state of S in apatite may serve as a proxy to reconstruct redox and degassing processes in magmatic and magmatic-hydrothermal environments.

To our knowledge there is no published spectroscopic evidence or constraints on the oxidations states of S, other than S^{6+} (Paris et al., 2001), in apatite over the wide range

This is a preprint, the final version is subject to change, of the American Mineralogist (MSA)
Cite as Authors (Year) Title. American Mineralogist, in press.
(DOI will not work until issue is live.) DOI: http://dx.doi.org/10.2138/am-2017-5907

of fO_2 conditions that prevail in terrestrial magmatic systems (i.e., from fO_2 of FMQ to FMQ+4; Carmichael, 1991; Richards, 2014). Micro XANES spectroscopy at S *K*-edge is an *in situ,* high-resolution, non-destructive and sensitive technique used to probe the electronic and chemical structure (i.e., oxidation state) of S-bearing materials (Paris et al., 2001; Fleet 2005; Jugo et al., 2010). As a result, S XANES serves as a powerful technique that can be used to investigate the relationship between the oxidation state of S in apatite and co-existing melt. In this study, we apply XANES to investigate the S oxidation state in natural apatites as well as in experimentally grown apatite and co-existing silicate melt, with one potential outcome being the development of a S in apatite oxy-sulfo-barometer used to probe the fO_2 and fS_2 of magmatic systems.

GEOLOGIC BACKGROUND

Mina Carmen apatite

The Mina Carmen iron oxide apatite (IOA) deposit is located ~20 km E of the Atacama fault system in northern Chile (26.346993°S; 70.143110°W). The deposit is hosted within porphyritic andesite of the Los Cerros Florida formation and is dominated by massive iron oxide ore bodies consisting of magnetite and patches of modally minor hematite and minor apatite (Treloar and Colley, 1996). Apatite occurs as coarse-grained crystals up to 50 cm in length within the magnetite matrix and also within planar zones of magnetite.

Halogen (F, Cl, OH) and volatile (S) element zonation observed in Carmen apatite (Treloar and Colley, 1996; this study; Supplemental Data 1) is interpreted to represent primary magmatic fluorapatite that was subsequently metasomatically overprinted to

This is a preprint, the final version is subject to change, of the American Mineralogist (MSA)
Cite as Authors (Year) Title. American Mineralogist, in press.
(DOI will not work until issue is live.) DOI: http://dx.doi.org/10.2138/am-2017-5907

chlorapatite (ap-X_{Cl} > ap-X_F) by a meteoric H_2O-HCl-rich, HF-poor volatile phase. The presence of secondary REE-phosphate (e.g., monazite; [Ce,La,Th]PO_4) inclusions in Carmen apatites serve as textural evidence for chemical alteration via metasomatism (Harlov et al., 2015; this study). The fluid could be of magmatic (Piccoli and Candela, 2002) or non-magmatic origin (e.g., Barton and Johnson, 1996). Carmen apatite represents the hydrothermal (metasomatized) end-member of the apatites analyzed in this study.

Durango apatite

The IOA deposits near Durango, Mexico are hosted by silicic felsic volcanic rocks within the Carpintero Group (Lyons, 1988). There is general agreement that Durango apatites are magmatic-hydrothermal in origin (Piccoli and Candela, 2002). According to Lyons (1988), the low-Ti IOA deposits formed from a Fe-rich magmatic-hydrothermal fluid that evolved from felsic silicate magma following introduction of CO_2 into the magma from carbonate wall rocks. The initially single phase magmatic-hydrothermal fluid unmixed during decompression into a low-density vapor and higher-density liquid. Strong partitioning of F and Cl into the vapor phase increased the acidity of the vapor and the solubility of Fe as $FeCl_2$, and allowed significant iron oxide mineralization to occur when the vapor vented to the atmosphere and iron oxide precipitated from the Cl-rich liquid. Fluorapatite precipitated from the F-enriched vapor and is abundant in breccias and vapor cavities within the sheeted flows and flow breccia that formed the volcanic dome (Lyons, 1988). An alternative model for the formation of Durango apatite invokes non-magmatic fluids (e.g., Barton and Johnson , 1996).

This is a preprint, the final version is subject to change, of the American Mineralogist (MSA)
Cite as Authors (Year) Title. American Mineralogist, in press.
(DOI will not work until issue is live.) DOI: http://dx.doi.org/10.2138/am-2017-5907

Durango apatite grains from Cerro de Mercado, Mexico (Young et al., 1969; Lyons 1988), are frequently used as a fluorapatite standard (Jarosewich et al., 1980) that contains ~1,400 ±10% μg/g S and is considered to be chemically homogenous in regards to major elements. However, electron probe microanalysis (EPMA) of a Durango grain orientated where the c-axis is parallel to the incoming electron beam, yielded S totals averaging 875 ± 17 μg/g (1σ standard deviation; see Supplemental Data 2), indicating homogeneity in terms of S distribution within a single grain, but grain-to-grain variations in S content throughout the deposit.

METHODS

Crystallization experiments

Apatite crystallization experiments were conducted in rapid quench internally heated pressure vessels (IHPV) at Leibniz University Hannover (LUH), Germany. Gold capsules (3.8 mm O.D., 0.12 mm wall thickness, 10 mm length) were loaded with ~40 mg of mafic starting material (natural lamproite: Vestfjella, Dronning Maud Land, Antarctica; fused overnight at 1,200°C at ~FMQ+1.2 in a gas-mixing furnace; see Table 1) and 7-8 wt.% H_2O, in order to promote crystal growth of apatite. This composition was selected for our experiments because preliminary (unpublished) crystallization experiments showed that [1] it crystallizes homogeneous apatite, large enough for XANES and EPMA (~10 μm in diameter) and [2] it can dissolve significant amounts of S even under reducing conditions (cf., thermodynamic model of Liu et al., 2007). Here, the latter is important to reach S contents in apatite that are high enough for accurate EPMA and XANES analyses, even under reducing conditions where the apatite-melt partition

This is a preprint, the final version is subject to change, of the American Mineralogist (MSA)
Cite as Authors (Year) Title. American Mineralogist, in press.
(DOI will not work until issue is live.) DOI: http://dx.doi.org/10.2138/am-2017-5907

coefficient ($D_S^{ap/m}$) for S is less than unity (see Supplemental Data 3). Assemblages were loaded with either [a] ~1 wt.% pyrrhotite ($Fe_{1-X}S$; Sudbury, Ontario) or [b] ~0.35 wt.% elemental S + ~0.92 wt.% Fe_2O_3 (i.e., an Fe/S ratio corresponding to pyrrhotite) as the source of S, depending on the final fO_2 of the experiment. This procedure of adding S to the systems ensures similar bulk compositions for all runs, while ensuring that the oxidation state of S in the mixture is close to the S oxidation state prevailing at the experimental redox conditions in order to minimize the time required to reach redox equilibrium throughout the sample. We note that even without this step, equilibrium in terms of fO_2 between the vessel and the center of the capsule should be reached within a few hours (cf., Fiege et al., 2014).

The capsules were weighed, welded shut and placed in a drying oven (110-120°C) for several hours, then re-weighed to check for water loss. Charges were pressurized to ~60 MPa and rapidly decompressed to verify the mechanical integrity of the capsule. Lamproite experiments were run at 1000°C and 300 MPa for 3-5 days at three different imposed and controlled oxidation states, where fO_2 (log (fO_2/bar) = FMQ, FMQ+1.2, and FMQ+3 (FMQ = fayalite-magnetite-quartz solid buffer). For experiments conducted at FMQ and FMQ+1.2, the fO_2 within the IHPV was controlled by adding H_2 to the Ar-pressure medium and was monitored using a Shaw-membrane, while the most oxidized experiment was intrinsically buffered by the IHPV at FMQ+3 by using pure Ar gas (Berndt et al., 2002; Bell et al., 2011). The experiments were terminated by isobaric rapid quench. The capsules were re-weighed. Capsules revealing loss of weight (i.e., of volatiles/water) during any of the experimental steps were discarded. A list of experiments is provided in Table 2.

This is a preprint, the final version is subject to change, of the American Mineralogist (MSA)
Cite as Authors (Year) Title. American Mineralogist, in press.
(DOI will not work until issue is live.) DOI: http://dx.doi.org/10.2138/am-2017-5907

A photomicrograph of a representative run product is presented in Figure 1. Hexagonal apatite grains typically measure ~10 μm in diameter. The major crystalline phases in the quenched experimental run products were identified using an optical microscope and backscatter electron (BSE) imaging. The phase assemblages include apatite, clinopyroxene, amphibole, ±sulfide (e.g., depending on the prevailing fO_2 of the experiment) and co-existing silicate glass.

Natural samples

To better evaluate and apply the new experimental and analytical results presented here, we used a combination of EPMA, X-ray fluorescence (XRF) mapping and S XANES to characterize natural apatite grains from Durango (Piccoli and Candela, 2002) and the magmatic-hydrothermal Mina Carmen iron oxide – apatite (IOA) ore deposit (Chile; Treloar and Colley, 1996).

ANALYTICAL APPROACH

Electron probe microanalysis (EPMA)

Natural apatites from Durango and Mina Carmen, and experimental glasses and apatites were quantitatively characterized by wavelength dispersive EPMA using a CAMECA SX-100 at the University of Michigan (UM, Ann Arbor, USA), at the American Museum of Natural History (AMNH, New York, USA) and at LUH. An acceleration voltage of 15 keV, a beam current of 5-10 nA and a beam size of 5-10 μm beam was used for EPMA of the co-existing silicate glass. Peak counting times of 10 seconds were used for major and trace elements, except 5 seconds for Na and 60-240

seconds for S. An acceleration voltage of 15 keV, a beam current of 10 nA and a beam size of 2 μm was used for all element analysis of apatite. Peak counting times of 20 seconds were used for the major and trace elements, except 5 seconds for F and 60 seconds for S. Precautions were taken to prevent electron beam damage of apatites (e.g., halogen migration; see Goldoff et al., 2012) and glass (e.g., diffusion of Na and Si, Al burn-in; Morgan and London, 2005). During analysis of experimental apatites, both SiO_2 and Al_2O_3 concentrations were monitored for contribution of surrounding glass and mineral phases. Analyses indicating a contribution of the glass were rejected.

Electron backscatter diffraction (EBSD)

The crystallographic orientations of experimental apatites were determined by EBSD using a Zeiss EVO 60 Variable Pressure scanning electron microscope (SEM) at AMNH. An accelerating voltage of 20 keV was used under a low vacuum (~32 Pa). Samples were fine-polished using colloidal silicon and left uncoated for analysis. The EDAX TEAM software was used for processing and fitting and only results with a confidence index of ≥ 0.2 were considered.

Sulfur X-ray absorption near edge structures spectroscopy (S XANES)

In situ, S XANES measurements at the S *K*-edge were conducted at the GSECARS 13-ID-E beamline at Advanced Photon Source (APS), Argonne National Laboratory (USA). The beamline uses a high-flux beam ($\geq 4.5 \times 10^{10}$ photons/second/100 mA/mm^2) that is equipped to produce a high spatial resolution micro-focused 2x1 μm (μ-XANES) beam using Kirkpatrick-Baez (KB) focusing mirrors, and can cover an energy

This is a preprint, the final version is subject to change, of the American Mineralogist (MSA)
Cite as Authors (Year) Title. American Mineralogist, in press.
(DOI will not work until issue is live.) DOI: http://dx.doi.org/10.2138/am-2017-5907

range of 2.4 to 28 keV. The energy of the Si(111) channel cut monochromator was calibrated to the 2481.8 (±0.2) eV white line of the spectrum for Scotch™ Brand tape. Energy ranges were collected from 2450 to 2550 eV, with step sizes of 0.1-0.3 eV at the S *K*-edge (2464 to 2484 eV) and 1 eV for the pre-and-post edge regions using 0.5-3 second scan durations per energy step. Step scan durations of 1-3 seconds per energy step were used to analyze natural and experimental apatites to achieve higher S X-ray counts required for high-quality spectra, especially in low-S bearing apatites (e.g., <100 μg/g S).

The European Synchrotron Radiation Facility (ESRF) S *K*-edge XANES spectra database was used to identify the S^{6+} (~2482 eV; anhydrite), sulfite S^{4+} (~2478 eV; sodium sulfite) and sulfide S^{2-} (~2470 eV; pyrrhotite) peak energy positions for the unknowns (see Supplemental Data 4). All natural samples were analyzed via S XANES prior to EPMA, and experimental samples were re-polished extensively (following EPMA) to remove the upper few μm of each sample that may have been modified by electron beam irradiation damage produced during EPMA (see Wilke et al., 2008).

Glasses: Assessing beam damage systematics

Beam damage to hydrous glasses caused by X-ray irradiation has been observed by Wilke et al. (2008) and requires careful monitoring during analysis, especially for beamlines that use a high-flux X-ray beam such as 13-ID-E at APS. A method similar to the one described by Fiege et al. (2014) was used to measure glasses where several short scan durations (e.g., 0.5 seconds/energy step) were used to analyze the experimental hydrous mafic glasses and the spectra were monitored for beam damage related to photo-reduction effects resulting in the systematic reduction of the S^{6+} peak and subsequent

This is a preprint, the final version is subject to change, of the American Mineralogist (MSA)
Cite as Authors (Year) Title. American Mineralogist, in press.
(DOI will not work until issue is live.) DOI: http://dx.doi.org/10.2138/am-2017-5907

development of a S^{4+} peak (see Supplementary Figure 1; Métrich et al., 2002, 2009; Wilke et al., 2008; Jugo et al., 2010). This method has been proven to produce high quality spectra in hydrous glasses with S content of ~50 μg/g S. Whenever possible, spectra exhibiting evidence for beam damage (e.g., systematic photo-reduction of S^{6+} peak to S^{4+}; see Supplemental Figure 1; Wilke et al., 2008 and Jugo et al., 2010) were rejected and the remaining spectra were merged. However, the run at FMQ+1.2 was particularly prone to irradiation damage and even the first analysis contains a small but distinct S^{4+} feature, which is marked accordingly in the respective figures (*note:* considering that this peak is growing with exposure time, it is safe to assume that the S in this glass was all S^{6+} prior to XANES analyses; see Results section).

S XANES spectra correction and peak area integration

The X-ray absorption spectroscopy (XAS) data software analysis package Athena (Ifeffit package; Ravel and Newville, 2005) was used to first merge and subsequently normalize the raw spectra. Normalization of merged raw spectra involves setting the pre-edge and post-edge to 0 and 1, respectively. Merged and normalized spectra of samples with low S contents (e.g., <100 μg/g S) were smoothed in Athena using Gaussian 11 and 4 type filters.

The curve and peak fitting open source software Fityk (Wojdyr, 2010; version 0.9.8) was used for peak area integration analysis of merged, non-smoothed, and corrected spectra. The Fityk software provides information including the [a] peak intensity, [b] integrated peak areas, and [c] peak positions of the Gaussian functions. An exponentially modified Gaussian (EMG) function was used to fit the background to

This is a preprint, the final version is subject to change, of the American Mineralogist (MSA)
Cite as Authors (Year) Title. American Mineralogist, in press.
(DOI will not work until issue is live.) DOI: http://dx.doi.org/10.2138/am-2017-5907

277 eliminate contribution from the pre-and-post edges. The inflection point of the EMG
278 function was positioned at energies of ~2478-2480 eV for all spectra, and the pre-and-
279 post edges of the EMG function are at 0 and 1, respectively. Gaussian area (e.g.,
280 Gaussian-A) functions were used to separately fit the S^{6+}, S^{4+}, S^{2-} and ionization peak(s)
281 (Figure 2). The residual of the fitting when subtracting from the raw spectrum as a
282 function of energy was used to evaluate the fitting functions at the S *K*-edge (~2468-2484
283 eV; Figure 2).

284 The peak area ratios of the S^{6+}, S^{4+}, S^{2-} peaks were used to evaluate relative
285 changes in the oxidation state of S in the sample. Since all natural and experimental
286 apatites analyzed in this study contained S^{6+}, the integrated S^{6+}/S_{Total} peak area ratios (e.g.,
287 $S_{Total} = (S^{6+} + S^{4+} + S^{2-})$) were used in order to remain comparable between oxidized
288 (FMQ+3), intermediate (FMQ+1.2) and reduced (FMQ) redox systems (see
289 Supplemental Data 5). We stress that until a calibration using standards with known S^{6+},
290 S^{4+}, S^{2-} ratios is developed, the S^{6+}, S^{4+}, S^{2-} integrated peak area ratios measured in the
291 samples do not directly correspond to the actual S^{6+}, S^{4+}, S^{2-} ratio in the sample. This
292 integrated peak area ratio fitting approach deviates from the method developed by Jugo et
293 al. (2010), which does not consider the sharp S^{2-} peak, the S^{4+} peak, the ionization peak,
294 and does not apply a background subtraction. Here, the background subtraction is of
295 particular importance considering the low integrated intensity of the sulfite peak, and a
296 similar method has proven to be a reliable approach for high precision Fe oxidation state
297 analyses via XANES (e.g., Cottrell et al., 2009; Fiege et al., 2016). The integrated peak
298 area ratio method, as utilized in the current study, allows for peak modeling that is more
299 sensitive to these contributions, where calibration can serve as a consistent and accurate

This is a preprint, the final version is subject to change, of the American Mineralogist (MSA)
Cite as Authors (Year) Title. American Mineralogist, in press.
(DOI will not work until issue is live.) DOI: http://dx.doi.org/10.2138/am-2017-5907

method to quantify the S^{6+}, S^{4+}, and S^{2-} in apatite and co-existing glass (please note the high external precision of our method illustrated in Figures 3 and 4).

Time series and line transect measurements on Durango apatite

Sulfur XANES line transects and time series were collected on Durango apatite in order to evaluate the susceptibility or resistance of apatite to beam damage (e.g., photo-reduction effects; Wilke et al., 2008; Jugo et al., 2010) during exposure to a relatively high-flux X-ray beam during S XANES analysis. Time series measurements on Durango fluorapatite using analytical durations ranging from ~2 to 60 minutes per analytical spot produced insignificant variation (e.g., within analytical uncertainty) between the spectra (see Figure 3). Thus, irradiation damages resulting in a possible oxidation or reduction of S in apatite during the analyses can be ruled out.

Analysis of Durango apatite over a ~3,000 μm line transect (e.g., 100 μm step lengths and 2 scans per step) was performed (approximately parallel to the c-axis) to determine if the oxidation state of S is homogeneous throughout the grain. Following S XANES analysis, an EPMA line transect (see Supplemental Data 2) was performed parallel (within ~25 μm) to the S XANES analysis to measure possible variability in S concentration along the line transect. In Figure 4, we illustrate that the variability within the integrated S^{6+}/S_{Total} peak area ratios collected during S XANES analysis is within 10% analytical error and likely reflects the minor compositional heterogeneity with respect to S. We emphasize that we observed a quite significant grain-to-grain variability in S (~900 to ~1400 ppm S), whereas S^{6+}/S_{Total} peak area ratios remain at a constant value of 0.955 ±0.002 (2σ standard error). Hence, we suggest that Durango apatite is a suitable reference

This is a preprint, the final version is subject to change, of the American Mineralogist (MSA)
Cite as Authors (Year) Title. American Mineralogist, in press.
(DOI will not work until issue is live.) DOI: http://dx.doi.org/10.2138/am-2017-5907

material for S XANES analyses of (oxidized) apatites, but should be used with caution as a S concentration standard owing to the approximately 50% variability in measured S contents (this study).

XANES and EPMA line transects measurements on Mina Carmen apatite

A ~40 μm long S XANES line transect across hydrothermally altered (i.e., metasomatized) apatite from the Mina Carmen IOA deposit (Chile; Treloar and Colley, 1996) was performed to assess S speciation in S-rich areas adjacent to volatile-bearing cavities (S-rich areas were located via XRF mapping). The transect was collected near (within ±10-15 μm) a formerly volatile bearing (fluid/vapor) cavity towards the non-metasomatized region of the apatite grain (Figure 5). A parallel EPMA line transect was recorded ~10 μm away from the XANES transect to investigate a possible co-variation between S oxidation state and S content in Mina Carmen apatite.

RESULTS

S oxidation states in Carmen apatite

Combined with an EPMA transect (see Supplemental Data 1) parallel to the S XANES transect, the metasomatized areas of the Mina Carmen apatite show distinct variations in the S-concentration and the integrated S^{6+}/S_{Total} peak area ratios of the S XANES spectra (Figure 6A). The integrated S^{6+}/S_{Total} peak area ratios varied from 0.982 to 0.993 (Figure 6B), depending on the proximity to volatile induced alteration of the apatite grain (see Figure 5). The EPMA transect reveals a ~2 orders of magnitude increase in S content from the non-metasomatized area of apatite (e.g., <55 μg/g S limit

This is a preprint, the final version is subject to change, of the American Mineralogist (MSA)
Cite as Authors (Year) Title. American Mineralogist, in press.
(DOI will not work until issue is live.) DOI: http://dx.doi.org/10.2138/am-2017-5907

of detection; EPMA) to the metasomatized area of apatite near a volatile-bearing cavity rim (e.g., >2,000 μg/g S; Figure 6B), which correlates inversely with the evolution of the S^{6+}/S_{Total} peak area ratios.

XANES results at reduced oxidation state: FMQ

The average XANES spectrum for experimental apatite crystallized from the reduced (LA45-IH1; FMQ) lamproitic glasses exhibit dominant S^{2-} (~2469 eV sharp peak and ~2476 eV broad peak) and S^{6+} (~2482 eV) peaks (Figure 7A). The integrated S^{6+}/S_{Total} peak area ratio was 0.168 at FMQ. The reduced lamproitic glass was dominated by S^{2-} based on peaks at ~2469 eV (sharp peak) and ~2476 eV (broad peak).

We highlight that we observed an influence of the crystallographic orientation of apatite on the S peak area ratios in the S XANES spectra collected on apatite from the reduced run products (i.e., at FMQ; see Figure 8 and discussion section about the crystallographic orientation). Hence, several apatites and co-existing glass spots were analyzed and merged (prior to baseline removal and intensity normalization) in order to achieve an average spectrum, representative for the bulk S oxidation states within each sample (see also Evans et al., 2014).

XANES results at intermediate oxidation state: FMQ+1.2

The XANES spectra for experimental apatite that crystallized from a lamproitic glass at intermediate redox conditions (FMQ+1.2) reveals a dominant sulfate peak (~2482 eV) and a minor sulfite (S^{4+}; ~2478 eV) peak, where the integrated S^{6+}/S_{Total} peak area ratio was 0.958 at FMQ+1.2 (LA45-IH7; Figure 7B).

This is a preprint, the final version is subject to change, of the American Mineralogist (MSA)
Cite as Authors (Year) Title. American Mineralogist, in press.
(DOI will not work until issue is live.) DOI: http://dx.doi.org/10.2138/am-2017-5907

The sulfur-speciation of lamproitic glasses from the intermediate (FMQ+1.2) experiment is dominated by S^{6+} by peak at ~2482 eV but also shows a minor sulfite (S^{4+}; ~2478 eV) peak (Figure 7B). To demonstrate that beam-induced modification of the measured oxidation state of S in the glass causes the formation of the sulfite peak, the scanning time was intentionally increased from 0.5 to 1 second/energy step during analysis of the hydrous lamproitic glass from the intermediate fO_2 experiments. While using a scanning time of 1 second/energy step, the development and growth of the S^{4+} peak coupled with the simultaneous systematic depletion of the S^{6+} peak was observed during analysis, demonstrating the effects of beam damage due to X-ray irradiation (see Wilke et al., 2008). Thus, the XANES analyses indicate that S^{6+} is most probably the only, or at least the dominant, S species in the quenched glass at intermediate redox conditions (FMQ+1.2).

XANES results at oxidized oxidation state: FMQ+3

Dominant sulfate (~2482 eV) and minor sulfite (S^{4+}; ~2478 eV) peaks are observed in the spectra of apatites crystallized from the oxidized (FMQ+3) lamproitic glass (Figure 7C), where the integrated S^{6+}/S_{Total} peak area ratio was 0.963 at FMQ+3.The sulfur-speciation of lamproitic glasses from the oxidized (FMQ+3) experiment is dominated by S^{6+} based on the strong peak at ~2482 eV and the absence of S^{2-} peaks (i.e., ~2469 eV sharp peak and ~2476 eV broad peak; Figure 7C). Under short scanning times (0.5 second/energy step), the presence or systematic growth of a S^{4+} peak at ~2478 eV with analytical time was not observed; whereas increasing the scanning time to 1

This is a preprint, the final version is subject to change, of the American Mineralogist (MSA)
Cite as Authors (Year) Title. American Mineralogist, in press.
(DOI will not work until issue is live.) DOI: http://dx.doi.org/10.2138/am-2017-5907

second/scan would probably result in beam damage similar to that observed in the intermediate glass (LA45-IH7; Figure 7B).

DISCUSSION

S oxidation state in apatite as a function of fO_2

Sulfur XANES analyses of experimental apatite crystallized over a range of fO_2 conditions (FMQ, FMQ+1.2 and FMQ+3) reveals variability in S oxidation states in apatite as a function of the redox conditions of the system. To our knowledge, these data represent the first S XANES measurements demonstrating the substitution of S^{2-}, S^{4+} and S^{6+} in apatite or in any other naturally occurring mineral. Our observations are in agreement with recent quantum mechanical calculations that assess incorporation of S^{2-}, S^{4+} and S^{6+} in apatite (Kim et al., this volume).

The co-variation of the S content and the S oxidation state observed near a fluid cavity in Mina Carmen apatite (Figure 6B) is most plausibly explained by the metasomatic enrichment of S in apatite via reaction with a S-bearing (e.g., SO_2) fluid or vapor (Harlov, 2015). Here, the increasing S^{4+} fraction (decreasing S^{6+}/S_{Total}) indicates [1] that the fluid was relatively oxidized (high SO_2/H_2S ratio) and [2] that the S oxidation state remains to some extent unchanged as S partitions from from an oxidized fluid (SO_2) into an apatite (SO_3^{2-}; see discussion below about substitution mechanisms). There is likely no effect on the oxidation state of the fluid during the interaction with apatite, considering the elevated S contents expected of such fluids (e.g., Zajacz et al., 2012; Burgisser et al., 2015; Fiege et al., 2015).

This is a preprint, the final version is subject to change, of the American Mineralogist (MSA)
Cite as Authors (Year) Title. American Mineralogist, in press.
(DOI will not work until issue is live.) DOI: http://dx.doi.org/10.2138/am-2017-5907

Crystallographic orientation controls on S oxidation states in apatite

A co-variation of S oxidation states (mainly S^{6+} and S^{2-}) is observed in the apatites crystallized from the reduced (FMQ) lamproitic melts (Figure 8). These relative changes in S^{6+} and S^{2-} peak intensities are interpreted to be a function of the orientation of the crystal (e.g., parallel or perpendicular to the c-axis). Crystallographic orientation effects, i.e., variation in speciation as a function of crystallographic orientation, have been observed during Fe XANES analysis in various minerals (e.g., pyroxenes, amphiboles, micas and biotite; Dyar et al., 2002; Evans et al., 2014). This interpretation is entirely consistent with theoretical findings made by Kim et al. (this volume), suggesting the sulfide (probably as S^{2-}) sits on the column anion site whereas sulfate (SO_4^{2-}) and sulfite (SO_3^{2-}) are probably positioned within the phosphate (PO_4^{3-}) anion site. Moreover, a minor contribution of S^{4+} is indicated in spectra that are rather S^{6+} dominated and S^{2-} deficient (compare Figure 8C and 8D). Here, the absence of a S^{4+} peak in S^{2-} dominant spectra is probably related to the relative abundance of S^{2-} versus S^{4+}, i.e., we suggest that the S^{2-} peaks obscure the minor S^{4+} peak in most spectra.

Although crystallographic orientation effects were not observed in the apatites crystallizing from the intermediate (FMQ+1.2) and oxidized melts (FMQ+3), we cannot exclude the possibility of orientation effects, considering that the S^{4+} contribution to the spectra is small and possible changes in the S^{6+}/S_{Total} peak area ratio related to crystal orientation might be below detection limit.

Electron backscatter diffraction (EBSD) was performed to determine the orientation of the experimental apatites in the reduced samples (LA45-IH1) following XANES analysis (e.g., to avoid potential beam damage from electron beam irradiation).

This is a preprint, the final version is subject to change, of the American Mineralogist (MSA)
Cite as Authors (Year) Title. American Mineralogist, in press.
(DOI will not work until issue is live.) DOI: http://dx.doi.org/10.2138/am-2017-5907

Due to the complexity of the experimental (e.g., high crystallinity) samples, we were unable to positively correlate the measured crystallographic orientation of apatite crystals via EBSD with the apatite crystals measured with S XANES. However, EBSD generally confirmed that elongated apatites were analyzed with the electron beam being nearly perpendicular to the c-axis, and hexagonal shaped apatites were measured with the beam being approximately parallel to the c-axis (Figure 8). Hence, our results provide first-order evidence that S^{2-} and S^{6+} are incorporated into different locations within the apatite structure. While it is impossible to speculate about the possible location of S^{2-}, S^{4+} and S^{6+} within the apatite structure based on our analyses, we emphasize that Kim et al. (this volume) came to the same conclusion by ab initio modeling of the apatite structure, suggesting that S^{2-} is positioned in the (F^-, Cl^-, OH^-) anion site, while S^{4+} and S^{6+} are positioned in the phosphate site.

S in apatite substitution mechanisms

Several individual substitution mechanisms for S^{6+} have been proposed (cf., Parat et al., 2011). In REE-free systems, Rouse and Dunn (1982) and Parat et al. (2011A and 2011B) proposed exchange reactions involving Si and S, where: $2P^{5+} \Leftrightarrow S^{6+} + Si^{4+}$. Parat and Holtz (2005) performed apatite crystallization experiments in REE-free systems and confirmed the exchange reactions involving Na and S (Liu and Comodi, 1993; Parat and Holtz, 2004), where: $P^{5+} + Ca^{2+} \Leftrightarrow S^{6+} + Na^+$. In natural systems, which generally contain REEs, they can be incorporated via coupled exchange reactions (Streck and Dilles 1998; Tepper and Kuehner 1999; Parat et al. 2008; Pan and Fleet, 2002) such as:

$$2Ca^{2+} \Leftrightarrow REE^{3+} + Na^+ \quad [3]$$

This is a preprint, the final version is subject to change, of the American Mineralogist (MSA)
Cite as Authors (Year) Title. American Mineralogist, in press.
(DOI will not work until issue is live.) DOI: http://dx.doi.org/10.2138/am-2017-5907

460 $$P^{5+} + Ca^{2+} \Leftrightarrow REE^{3+} + Si^{4+}$$ [4]

461 Sulfur XANES analyses (this study) indicate that S^{6+} and S^{4+} co-exist in experimental
462 apatites that crystallized from intermediate to oxidized conditions (e.g., FMQ+1.2 to 3).
463 Considering the $2P^{5+} \Leftrightarrow S^{6+} + Si^{4+}$ substitution, a mechanism involving:

464 $$2P^{5+} \Leftrightarrow S^{6+} + S^{4+}$$ [5]

465 is most plausible and consistent with computational results from Kim et al. (this volume).
466 A plausible explanation for the incorporation of S^{4+} into apatite is via a local redox
467 reaction involving the reduction of S^{6+} to S^{4+}, where:

468 $$SO_4^{2-}{}_{(melt)} \Leftrightarrow SO_3^{2-}{}_{(apatite)} + \frac{1}{2}\, O_{2\,(melt)}$$ [6]

469 This redox reaction scenario is favored since [a] it does not require a significant
470 contribution of S^{4+} from the melt and [b] S^{4+} incorporation into the apatite structure may
471 serve as a mechanism to charge balance the incorporation of S^{6+} (see Kim et al., this
472 volume).

473 Notably, for Fe-free and Fe-poor (≤ 1.6 wt% FeO) silicic melts, Métrich et al.
474 (2009) observed a minor S^{4+} peak, which is probably unrelated to irradiation effects. The
475 authors suggest that S^{4+} is not stable in the glass structure, but stable in melts at elevated
476 P-T. Hence, a possible but unlikely scenario (considering the elevated Fe contents in the
477 lamproitic melt) could be that the S oxidation state in apatite indeed reflects the
478 speciation in the melt from which apatite crystallizes.

479 Although the presence of S^{2-} in natural apatites has never been directly measured
480 spectroscopically, Henning et al. (2000) successfully synthesized calcium sulfoapatite
481 ($Ca_5(PO_4)_3S$) and argued that sulfoapatites are not capable of absorbing H_2S into their
482 structure the way that oxyapatites can absorb H_2O at elevated temperatures, owing to the

This is a preprint, the final version is subject to change, of the American Mineralogist (MSA)
Cite as Authors (Year) Title. American Mineralogist, in press.
(DOI will not work until issue is live.) DOI: http://dx.doi.org/10.2138/am-2017-5907

position of the sulfide (S^{2-}) ion. This observation, which is in good agreement with the S XANES spectra of apatites crystallizing under reducing conditions (FMQ; Figure 7A), provides an important constraint on the substitution mechanisms associated with S^{2-} in the apatite structure; e.g., under reducing conditions, S^{2-} is likely more favorable within the apatite structure compared to HS^- (Henning et al., 2000; Kim et al., this volume). Notably, in the reduced experimental systems (FMQ; this study), apatites are S-bearing (up to ~320 μg/g S) and are characterized stoichiometrically as hydroxyl-fluorapatite (ap-X_{OH} > ap-X_F >> ap-X_{Cl}). The results of Kim et al. (this volume) also suggest that the incorporation of S^{2-} plus a lattice vacancy favors 2Cl > 2OH > 2F, suggesting that S^{2-} is increasingly stable when: ap-X_{Cl} > ap-X_{OH} > ap-X_F.

Finally, we speculate that the increasing S^{4+} fraction (decreasing S^{6+}/S_{Total}) observed in Mina Carmen apatite indicates that a sulfate-sulfite coupled substitution mechanism is dominant during hydrothermal alteration of apatite by a relatively oxidizing fluid/vapor. Here, a reaction involving: $2PO_4^{3-}{}_{(apatite)} + 2SO_{2\,(fluid)} + 1½\ O_{2\,(fluid)} \Leftrightarrow SO_4^{2-}{}_{(apatite)} + SO_3^{2-}{}_{(apatite)} + 2PO_4^{3-}{}_{(fluid)}$, plausibly explains the incorporation of S^{6+} and S^{4+} in apatite during reaction with a SO_2-bearing fluid phase.

IMPLICATIONS

The oxidation state of S as a function of fO_2 plays a crucial role in controlling the solubilities of S and (chalcophile) ore metals in silicate melts as well as the partitioning of S and (chalcophile) ore metals between silicate melts and magmatic-hydrothermal fluids. We emphasize that the strong dependence of the S oxidation state in apatite as a function of fO_2 is also coupled with changing S contents in the apatite and the co-existing

This is a preprint, the final version is subject to change, of the American Mineralogist (MSA)
Cite as Authors (Year) Title. American Mineralogist, in press.
(DOI will not work until issue is live.) DOI: http://dx.doi.org/10.2138/am-2017-5907

506 melt, resulting in a complex correlation between [a] apatite-melt (or fluid) partitioning,
507 [b] redox conditions and [c] the melt and/or fluid composition. The presence of three S
508 oxidation states in apatite may in part, explain the non-Henrian distribution behavior of S
509 between apatite and co-existing melt (Parat et al., 2011).

510 Upon calibration over a range of geologically relevant T-P-X-fO_2-fS_2, our study
511 reveals that the oxidation state of S in apatite may serve as a powerful geochemical tool
512 that will allow geoscientists to quantify the fO_2 and fS_2 conditions of ore-forming
513 magmatic-hydrothermal and hydrothermal systems. However, the key for a robust
514 calibration will be the determination of incorporation mechanisms for S^{6+}, S^{4+}, and S^{2-} in
515 apatite, where the chemistry of the host apatite may introduce other controlling
516 parameters that complicate the calibration (Kim et al., this volume).

517

518 **ACKNOWLEDGMENTS**

519 We acknowledge the experimental and analytical facilities at Leibniz University
520 Hannover (LUH), University of Michigan (UM), American Museum of Natural History
521 (AMNH) and GeoSoilEnviroCars (Sector 13), Advanced Photon Source (APS), Argonne
522 National Laboratory. We thank M. Newville and T. Lanzarotti for assistance and
523 discussion during S XANES analysis. We also thank T. Hudgins, P. Ruprecht, N. La
524 Cruz for their assistance in data collection; S. Wilke, and O. Namur for their assistance
525 during experiments; and J. Knipping, T. Childress, M. Reich and F. Barra for collecting
526 the Carmen sample. This research used resources of the Advanced Photon Source, a U.S.
527 Department of Energy (DOE) Office of Science User Facility operated for the DOE
528 Office of Science by Argonne National Laboratory under Contract No. DE-AC02-

529 06CH11357. This work was funded by the NSF, EAR-grant #1524394. B.A.K
530 acknowledges support from Rackham Graduate School (UM) and a Society of Economic
531 Geologists Student Research Grant.

532

533 **CITATIONS**

534 Barton, M.D., and Johnson, D.A. (2000) Alternative brine sources for Fe-oxide (Cu-Au)
535 systems: Implications for hydrothermal alteration and metals: in T. M. Porter
536 (editor), Hydrothermal iron oxide copper-gold and related deposits a global
537 perspective. Australian Mineral Foundation, Glenside, South Australia, 43–46.
538 Bell, A.S., and Simon, A. (2011) Experimental evidence for the alteration of the
539 Fe3+/ΣFe of silicate melt caused by the degassing of chlorine-bearing aqueous
540 volatiles. Geology, 39, 499–502.
541 Berndt, J., Liebske, C., Holtz, F., Freise, M., Nowak, M., Ziegenbein, D., Hurkuck, W.,
542 and Koepke, J. (2002) A combined rapid-quench and H_2 –membrane setup for
543 internally heated pressure vessels: Description and application for water solubility
544 in basaltic melts. American Mineralogist, 87, 1717–1726.
545 Boyce, J.W., Liu, Y., Rossman, G.R., Guan, Y., Eiler, J.M., Stolper, E.M., and Taylor,
546 L.A. (2010) Lunar apatite with terrestrial volatile abundances. Nature, 466, 466–9.
547 Boyce, J.W., Tomlinson, S.M., McCubbin, F.M., Greenwood, J.P., and Treiman, a H.
548 (2014) The lunar apatite paradox. Science (New York, N.Y.), 344, 400–2.
549 Burgisser, A., Alletti, M., and Scaillet, B. (2015) Simulating the behavior of volatiles
550 belonging to the C–O–H–S system in silicate melts under magmatic conditions with
551 the software D-Compress. Computers & Geosciences, 79, 1–14.

552 Candela, P., and Piccoli, P. (2005) Magmatic Processes in the Development of Porphyry-
553 Type Ore Systems. Economic Geology, 25–37.
554 Carmichael, I.S.E. (1991) The redox states of basic and silicic magmas: a reflection of
555 their source regions? Contributions to Mineralogy and Petrology, 106, 129–141.
556 Dyar, M.D., Gunter, M.E., Delany, J.S., Lanzarotti, A.A., and Sutton, S.R. (2002)
557 Systematics in the structure and XANES spectra of pyroxenes, amphiboles, and
558 micas as derived from oriented single crystals. Canadian Mineralogist, 40, 1375–
559 1393.
560 Evans, K.A., Dyar, M.D., Reddy, S.M., Lanzirotti, A., Adams, D.T., and Tailby, N.
561 (2014) Variation in XANES in biotite as a function of orientation, crystal
562 composition, and metamorphic history. American Mineralogist, 99, 443–457.
563 Faure, G. (1986) Principles of Isotope Geology. John Wiley and Sons, New York, 589.
564 Fiege, A., Behrens, H., Holtz, F., and Adams, F. (2014) Kinetic vs. thermodynamic
565 control of degassing of H_2O–S±Cl-bearing andesitic melts. Geochimica et
566 Cosmochimica Acta, 125, 241–264.
567 Fiege, A., Holtz, F., Behrens, H., Mandeville, C.W., Shimizu, N., Crede, L.S., and
568 Göttlicher, J. (2015) Experimental investigation of the S and S-isotope distribution
569 between H_2O–S±Cl fluids and basaltic melts during decompression. Chemical
570 Geology, 393-394, 36–54.
571 Fiege A., Ruprecht P., Simon A., Bell A., Göttlicher J., Newville M., Lanzirotti T.,
572 Moore G. (2016) Calibration of Fe XANES for high-precision determination of Fe
573 oxidation state in glasses: Comparison of results obtained at different synchrotron
574 radiation sources. *American Mineralogist, in press*.

575 Fleet, M.E. (2005) Xanes spectroscopy of sulfur in earth materials. The Canadian
576 Mineralogist, 43, 1811–1838.
577 Goldoff, B., Webster, J.D., and Harlov, D.E. (2012) Characterization of fluor-
578 chlorapatites by electron probe microanalysis with a focus on time-dependent
579 intensity variation of halogens. American Mineralogist, 97, 1103–1115.
580 Gustafson, L.B., and Hunt, J.P. (1975) The porphyry copper deposit at El Salvador,
581 Chile. Economic Geology, 70, 857–912.
582 Harlov, D.E. (2015) Apatite: A Fingerprint for Metasomatic Processes. Elements, 11,
583 171–176.
584 Henning, P.A., Adolfsson, E., and Grins, J. (2000) The chalcogenide phosphate apatites
585 $Ca_{10(}PO_4)_6S$, $Sr_{10}(PO_4)_6S$, $Ba_{10}(PO_4)_6S$ and $Ca_{10}(PO_4)_6Se$. Zeitschrift für
586 Kristallographie - Crystalline Materials, 215, 105110.
587 Jarosewich, E., Nelen, J.A., and Norberg, J.A. (1980) Reference samples for electron
588 microprobe analysis. Geostandards Newsletter, 4, 43–47.
589 Jugo, P.J., Wilke, M., and Botcharnikov, R.E. (2010) Sulfur K-edge XANES analysis of
590 natural and synthetic basaltic glasses: Implications for S speciation and S content as
591 function of oxygen fugacity. Geochimica et Cosmochimica Acta, 74, 5926–5938.
592 Kim, Y.J., Konecke, B.A., Fiege, A., Simon, A.C., Becker, U. (----) An ab-initio study on
593 sulfur-bearing apatite: Energetics and geometry upon incorporation. American
594 Mineralogist, this volume, accepted pending revisions
595 Liu, Y., and Comodi, P. (1993) Some aspects of the crystal-chemistry of apatites.
596 Mineralogical magazine, 57, 709–719.

597 Liu, Y., Samaha, N.-T., and Baker, D.R. (2007) Sulfur concentration at sulfide saturation
598 (SCSS) in magmatic silicate melts. Geochimica et Cosmochimica Acta, 71, 1783–
599 1799.
600 Lyons, J.I. (1988) Volcanogenic iron oxide deposits, Cerro de Mercado and vicinity,
601 Durango. Economic Geology, 83, 1886–1906.
602 Mandeville, C.W. (2010) Sulfur: A Ubiquitous and Useful Tracer in Earth and Planetary
603 Sciences. Elements, 6, 75–80.
604 Mao, M., Rukhlov, A.S., Rowins, S.M., Spence, J., and Coogan, L.A. (2016) Apatite
605 Trace Element Compositions: A Robust New Tool for Mineral Exploration.
606 Economic Geology, 111, 1187–1222.
607 McCubbin, F.M., and Jones, R.H. (2015) Extraterrestrial Apatite: Planetary
608 Geochemistry to Astrobiology. Elements, 11, 183–188.
609 Métrich, N., Bonnin-Mosbah, M., Susini, J., Menez, B., and Galoisy, L. (2002) Presence
610 of sulfite (SIV) in arc magmas: Implications for volcanic sulfur emissions.
611 Geophysical Research Letters, 29, 4–7.
612 Métrich, N., Berry, A.J., O'Neill, H.S.C., and Susini, J. (2009) The oxidation state of
613 sulfur in synthetic and natural glasses determined by X-ray absorption spectroscopy.
614 Geochimica et Cosmochimica Acta, 73, 2382–2399.
615 Metrich, N., and Mandeville, C.W. (2010) Sulfur in Magmas. Elements, 6, 81–86.
616 Morgan, G., and London, D. (2005) Effect of current density on the electron microprobe
617 analysis of alkali aluminosilicate glasses. American Mineralogist, 90, 1131–1138.

618 Pan, Y., and Fleet, M.E. (2002) Compositions of the Apatite-Group Minerals:
619 Substitution Mechanisms and Controlling Factors. Reviews in Mineralogy and
620 Geochemistry, 48, 13–49.
621 Peng, G., Luhr, J., and McGee, J. (1997) Factors controlling sulfur concentrations in
622 volcanic apatite. American Mineralogist, 82, 1210–1224.
623 Parat, F., and Holtz, F. (2004) Sulfur partitioning between apatite and melt and effect of
624 sulfur on apatite solubility at oxidizing conditions. Contributions to Mineralogy and
625 Petrology, 147, 201–212.
626 Parat, F., and Holtz, F. (2005) Sulfur partition coefficient between apatite and rhyolite:
627 The role of bulk S content. Contributions to Mineralogy and Petrology, 150, 643–
628 651.
629 Parat, F., Holtz, F., and Feig, S. (2008) Pre-eruptive conditions of the Huerto Andesite
630 (Fish canyon system, San Juan volcanic field, Colorado): Influence of volatiles (C-
631 O-H-S) on phase equilibria and mineral composition. Journal of Petrology, 49, 911–
632 935.
633 Parat, F., Holtz, F., and Klügel, A. (2011A) S-rich apatite-hosted glass inclusions in
634 xenoliths from La Palma: constraints on the volatile partitioning in evolved alkaline
635 magmas. Contributions to Mineralogy and Petrology, 162, 463–478.
636 Parat, F., Holtz, F., and Streck, M.J. (2011B) Sulfur-bearing Magmatic Accessory
637 Minerals. Reviews in Mineralogy and Geochemistry, 73, 285–314.
638 Paris, E., Giuli, G., Carroll, M.R., and Davoli, I. (2001) The valence and speciation of
639 sulfur in glasses by x-ray absorption spectroscopy. Canadian Mineralogist, 39, 331–
640 339.

This is a preprint, the final version is subject to change, of the American Mineralogist (MSA)
Cite as Authors (Year) Title. American Mineralogist, in press.
(DOI will not work until issue is live.) DOI: http://dx.doi.org/10.2138/am-2017-5907

641 Piccoli, P.M., and Candela, P.A. (2002) Apatite in Igneous Systems. Reviews in
642 Mineralogy and Geochemistry, 48, 255–292.
643 Pokrovski, G.S., and Dubrovinsky, L.S. (2011) The S_3^- Ion Is Stable in Geological Fluids
644 at Elevated Temperatures and Pressures. Science, 331, 1052–1054.
645 Pokrovski, G.S., and Dubessy, J. (2015) Stability and abundance of the trisulfur radical
646 ion S_3^- in hydrothermal fluids. Earth and Planetary Science Letters, 411, 298–309.
647 Ravel, B., and Newville, M. (2005) ATHENA, ARTEMIS, HEPHAESTUS: Data
648 analysis for X-ray absorption spectroscopy using IFEFFIT. Journal of Synchrotron
649 Radiation, 12, 537–541.
650 Richards, J.P. (2014) The oxidation state, and sulfur and Cu contents of arc magmas:
651 Implications for metallogeny. Lithos, 233, 27–45.
652 Rouse, R.C., and Dunn, P.J. (1982) A contribution to the crystal chemistry of ellestadite
653 and the silicate sulfate apatites. American Mineralogist, 67, 90–96.
654 Sato, M., Hickling, N. L., McLane, J.E. (1973) Oxygen fugacity values of Apollo 12, 14,
655 and 15 lunar samples and reduced state of lunar magmas. Proceedings of the Lunar
656 Science Conference, 4, 1061–1079.
657 Simon, A.C., and Ripley, E.M. (2011) The Role of Magmatic Sulfur in the Formation of
658 Ore Deposits. Reviews in Mineralogy and Geochemistry, 73, 513–578.
659 Streck, M.J., and Dilles, J.H. (1998) Sulfur evolution of oxidized arc magmas as recorded
660 in apatite from a porphyry copper batholith. Geology, 26, 523.
661 Tepper, J., and Kuehner, S. (1999) Complex zoning in apatite from the Idaho batholith: A
662 record of magma mixing and intracrystalline trace element diffusion. American
663 Mineralogist, 84, 581–595.

664 Treloar, P.J., and Colley, H. (1996) Variation in F and Cl contents in apatites from
665 magnetite-apatite ores in northern Chile, and their ore-genetic implications.
666 Mineralogical Magazine, 60, 285–301.
667 Webster, J.D., and Piccoli, P.M. (2015) Magmatic Apatite: A Powerful, Yet Deceptive,
668 Mineral. Elements, 11, 177–182.
669 Wilke, M., Jugo, P.J., Klimm, K., Susini, J., Botcharnikov, R., Kohn, S.C., and Janousch,
670 M. (2008) The origin of S4+ detected in silicate glasses by XANES. American
671 Mineralogist, 93, 235–240.
672 Wojdyr, M. (2010) Fityk: A general-purpose peak fitting program. Journal of Applied
673 Crystallography, 43, 1126–1128.
674 Young, E.J., Myers, A.T., Munson, E.L and Conklin, N.M. (1969) Mineralogy and
675 geochemistry of fluorapatite from Cerro de Mercado, Durango, Mexico. USGS
676 Professional Paper 650-D, D84-D93.
677 Zajacz, Z., Candela, P. a., Piccoli, P.M., and Sanchez-Valle, C. (2012) The partitioning of
678 sulfur and chlorine between andesite melts and magmatic volatiles and the exchange
679 coefficients of major cations. Geochimica et Cosmochimica Acta, 89, 81–101.
680

681 **FIGURE CAPTIONS**

682 Figure 1: Backscatter electron (BSE) image of a representative area of experimental run
683 product LA45-IH1. The run product includes: quenched glass (gl), apatite (ap),
684 clinopyroxene (cpx), amphibole (amp), and ± iron sulfide (po; e.g., depending on the fO_2
685 of the system). Scale bar represents 20 μm.
686

This is a preprint, the final version is subject to change, of the American Mineralogist (MSA)
Cite as Authors (Year) Title. American Mineralogist, in press.
(DOI will not work until issue is live.) DOI: http://dx.doi.org/10.2138/am-2017-5907

687 Figure 2 A-D: Illustration of the Fityk peak fitting procedure for selected S XANES
688 spectra (merged; dotted lines) collected on apatites. (A) Durango apatite; (B) LA45-IH1
689 apatite (FMQ); (C) LA45-IH7 apatite (FMQ+1.2); (D) LA45-IH13 apatite (FMQ+3).
690 Gaussian-A functions (solid lines) were used to fit the S^{6+}, S^{4+}, S^{2-} and ionization peaks
691 and exponentially modified Gaussian (EMG) functions were used to fit the background
692 (dashed line). The integrated peak area ratios of the S^{6+}, S^{4+} and S^{2-} peaks were used in
693 order to evaluate relative changes in S-oxidation state in the sample, where: $S_{total} = (S^{6+} +$
694 $S^{4+} + S^{2-})$. The plots below A-D show the residual of the fitting when subtracting from the
695 raw spectrum as a function of energy. The black part of the lines represents the fitting at
696 the S *K-edge* (~2468-2484 eV), whereas the gray lines represent the non-fitted pre-and-
697 post edge.
698
699 Figure 3: One-hour S XANES time-series on Durango apatite to test for possible
700 irradiation damages potentially resulting in an oxidation or reduction of sulfur in apatite
701 during analysis. Twenty, 3-minute long scans were taken on the same analytical spot and
702 the integrated S^{6+}/S_{Total} peak area ratios were evaluated for significant deviation (e.g.,
703 within ±1σ standard deviation; gray box). The average (dashed line) integrated S^{6+}/S_{Total}
704 peak area ratio = 0.956 ±0.002 (2σ standard error). The determination of the integrated
705 S^{6+}/S_{Total} peak area ratios is described in the analytical approach section.
706
707 Figure 4: EPMA (triangles) and S XANES (circles) line transect (~3,000 μm; rim to rim)
708 on a grain of Durango apatite that was orientated approximately parallel to the c-axis.
709 The EPMA and S XANES line transects were performed parallel to each other within

This is a preprint, the final version is subject to change, of the American Mineralogist (MSA)
Cite as Authors (Year) Title. American Mineralogist, in press.
(DOI will not work until issue is live.) DOI: http://dx.doi.org/10.2138/am-2017-5907

710 ~50 μm distance. The average S content, 875 ± 17 μg/g (1σ standard deviation), is ~50%
711 lower than published values (Young et al., 1969) and may reflect either grain-to-grain
712 heterogeneity (see main text for discussion). The gray boxes represent 1σ standard
713 deviation of the average for each analysis. The average integrated S^{6+}/S_{Total} peak area ratio
714 = 0.955 ±0.002 (2σ standard error).
715
716 Figure 5: Backscatter electron (BSE) image of the volatile bearing cavity region of the
717 Mina Carmen apatite. The reacted (e.g., metasomatized) regions are denoted by the
718 medium gray, while the un-metasomatized the darker gray regions. The red arrow
719 indicates the approximate location (within ±10-15 μm) of the EPMA (See Supplemental
720 Data 1) and XANES transects.
721
722 Figure 6 A-B: Sulfur oxidation states and contents in Carmen apatite. (A) S XANES
723 spectra of Carmen apatite. The red solid line denotes the XANES scan at the edge of the
724 volatile cavity (e.g., metasomatized region; see Figure 5) and the black dotted line from
725 the scan ~40 μm away from the cavity (non-metasomatized region). (B) S XANES and
726 EPMA transect of Carmen apatite from the S-rich region near the cavity into the non-
727 metasomatized, S-poor region. The black dashed line represents the EPMA limit of
728 detection of ~55 μg/g. The gray triangles represent EPMA spot analysis below limit of
729 detection. Error bars are reported in 2σ standard error.
730
731 Figure 7 A-C: S XANES analysis of quenched glass (gl; top) and apatite (ap; bottom)
732 from experiments performed at different fO_2 conditions: (A) FMQ, (B) FMQ+1.2 and (C)

This is a preprint, the final version is subject to change, of the American Mineralogist (MSA)
Cite as Authors (Year) Title. American Mineralogist, in press.
(DOI will not work until issue is live.) DOI: http://dx.doi.org/10.2138/am-2017-5907

733 FMQ+3. The presented spectra are merged spectra, whereas spectra indicating beam
734 damage (only applicable for glasses) were excluded. (A) Under reducing redox
735 conditions (FMQ; LA45-IH1), only S^{2-} was observed in the co-existing glass, while S^{6+}
736 and S^{2-} (and possibly S^{4+}; see Figure 8) were observed in apatite. (B-C) Intermediate and
737 oxidizing redox conditions (e.g., fO_2=FMQ+1.2 and FMQ+3, LA45-IH7 and IH13,
738 respectively) revealed S^{6+} and S^{4+} co-existing in apatite that crystallized under
739 intermediate-oxidized redox conditions. Beam damage was observed even for the first
740 spectrum collected on one spot on the intermediate glass (B; FMQ+1.2), resulting in the
741 immediate formation of S^{4+}. However, the intermediate glass is interpreted to be fully
742 oxidized (all S^{6+}) prior to XANES analyses (see main text). All S in the oxidized glass (C;
743 FMQ+3) is present as S^{6+}.
744
745 Figure 8 A-D: S XANES spectra for apatite crystallized from reduced lamproitic melt
746 (LA45-IH1; FMQ) and separated by their perceived orientation relative to the surface.
747 (A) Partially parallel c-axis; (B) partially perpendicular to c-axis; (C) perpendicular to c-
748 axis; and (D) merged spectra of all apatites measured in the sample. Crystal geometries
749 were perceived optically during XANES analysis and due to the complexity of the
750 sample, the crystal orientations could only be correlated using EBSD. The approximate
751 qualitative interpretation of the orientation made during the XANES sessions was
752 generally confirmed by subsequent EBSD analyses (elongated crystals are measured
753 ~perpendicular to c-axis; hexagonal shaped crystals were measured ~parallel to c-axis);
754 see main text for details.
755

Supplemental Figure 1: Sulfur XANES spectrum of hydrous glass demonstrating beam damage, which is characterized by the systematic reduction of the S^{6+} peak and development of a S^{4+} peak with increasing analytical time (e.g., from scan 1 to scan 3).

This is a preprint, the final version is subject to change, of the American Mineralogist (MSA)
Cite as Authors (Year) Title. American Mineralogist, in press.
(DOI will not work until issue is live.) DOI: http://dx.doi.org/10.2138/am-2017-5907

Figure 1.

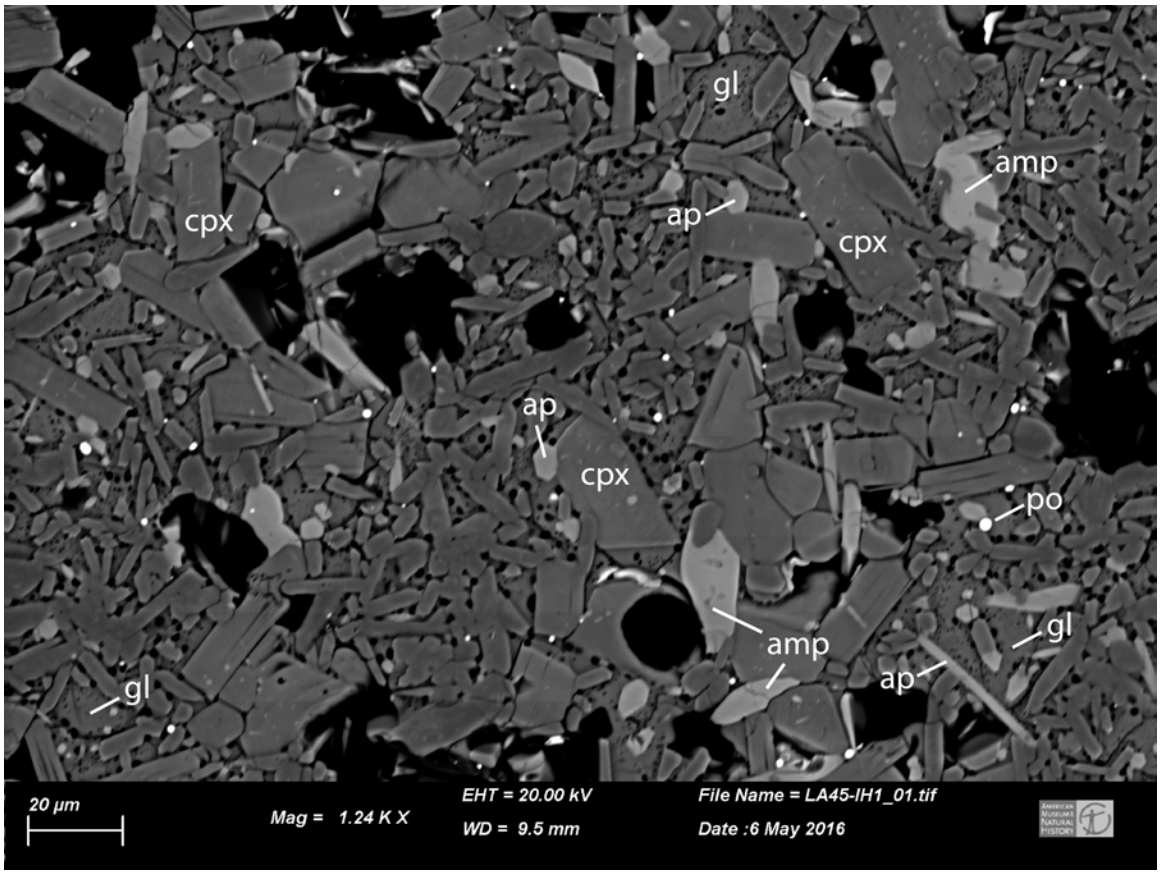

This is a preprint, the final version is subject to change, of the American Mineralogist (MSA)
Cite as Authors (Year) Title. American Mineralogist, in press.
(DOI will not work until issue is live.) DOI: http://dx.doi.org/10.2138/am-2017-5907

Figure 2.

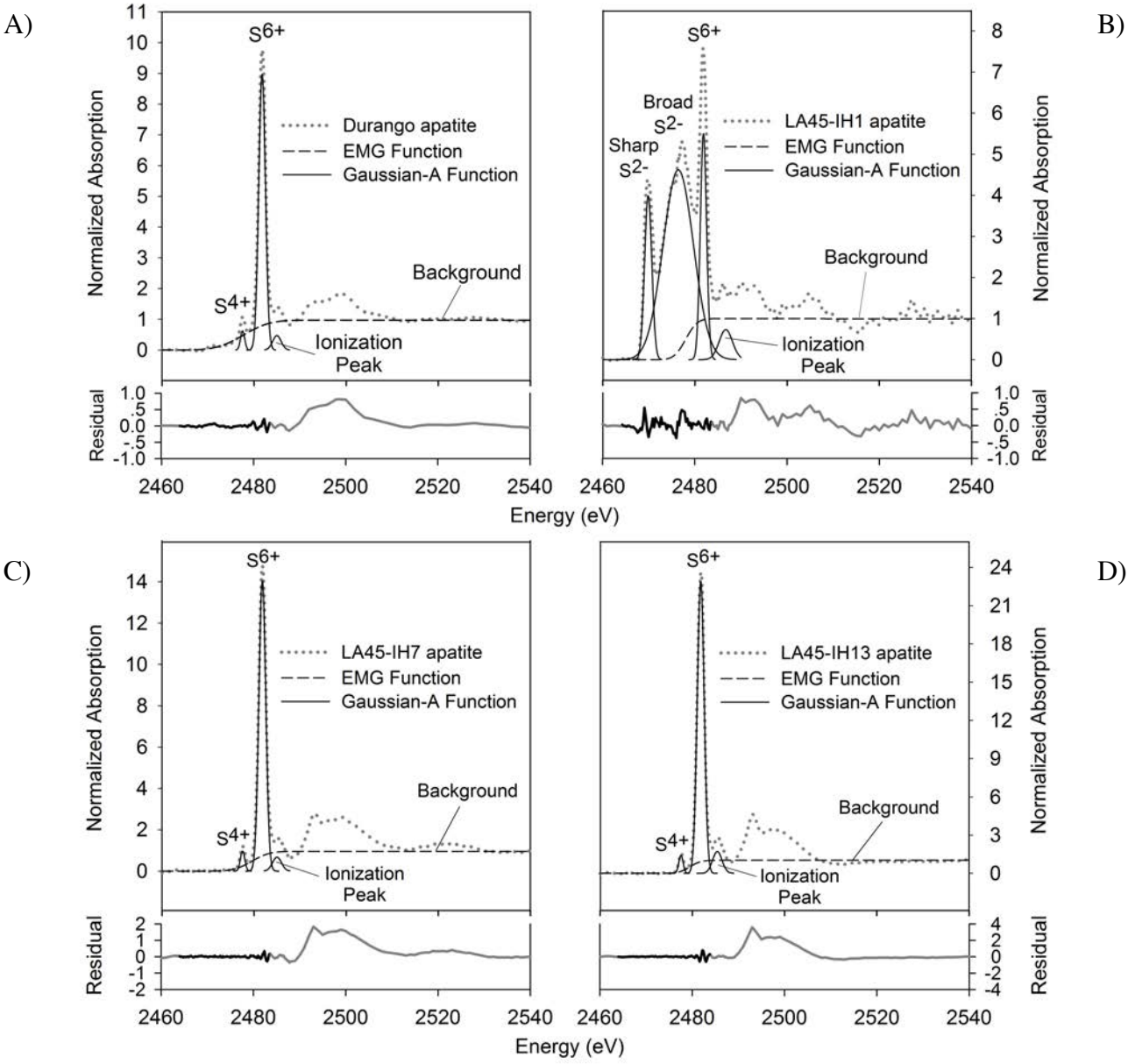

This is a preprint, the final version is subject to change, of the American Mineralogist (MSA)
Cite as Authors (Year) Title. American Mineralogist, in press.
(DOI will not work until issue is live.) DOI: http://dx.doi.org/10.2138/am-2017-5907

Figure 3.

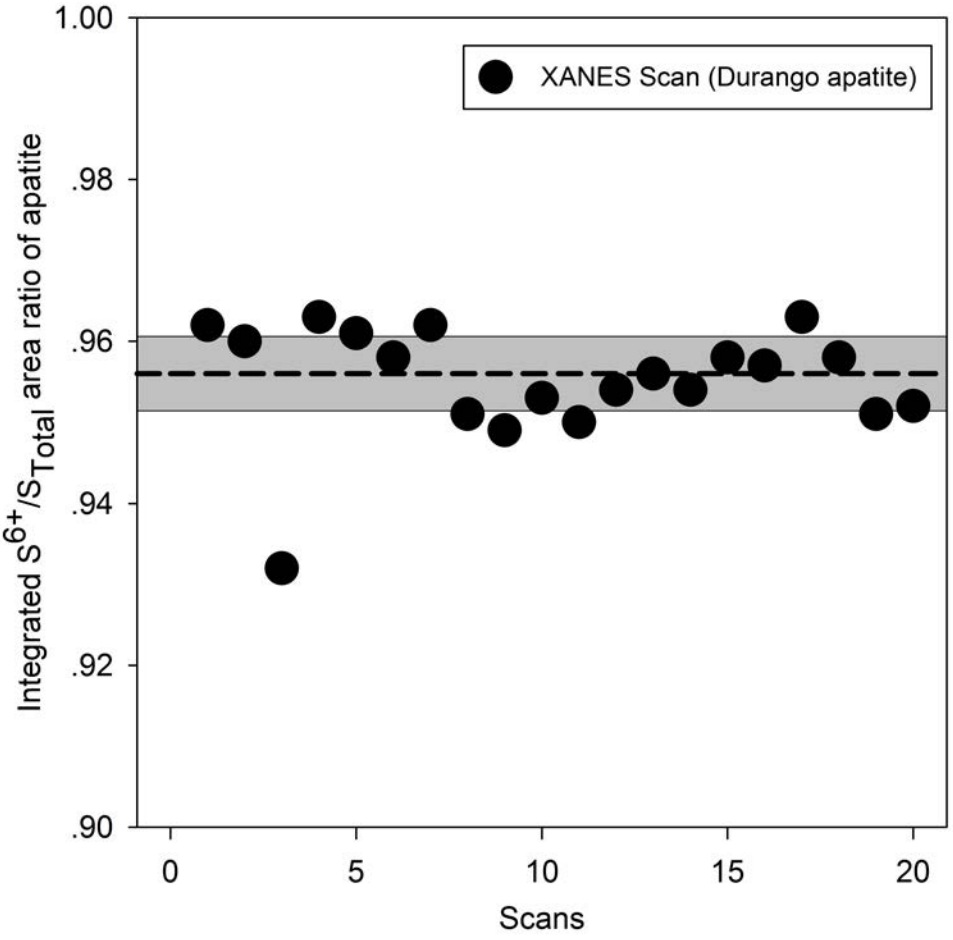

This is a preprint, the final version is subject to change, of the American Mineralogist (MSA)
Cite as Authors (Year) Title. American Mineralogist, in press.
(DOI will not work until issue is live.) DOI: http://dx.doi.org/10.2138/am-2017-5907

Figure 4.

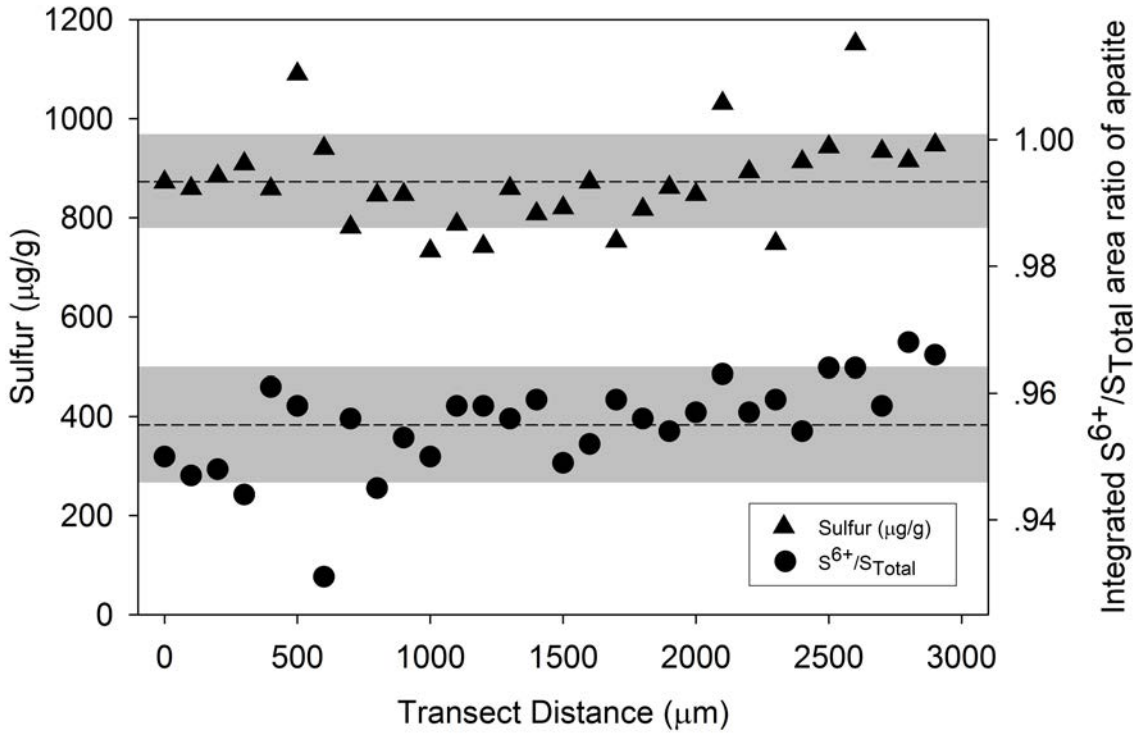

This is a preprint, the final version is subject to change, of the American Mineralogist (MSA)
Cite as Authors (Year) Title. American Mineralogist, in press.
(DOI will not work until issue is live.) DOI: http://dx.doi.org/10.2138/am-2017-5907

Figure 5.

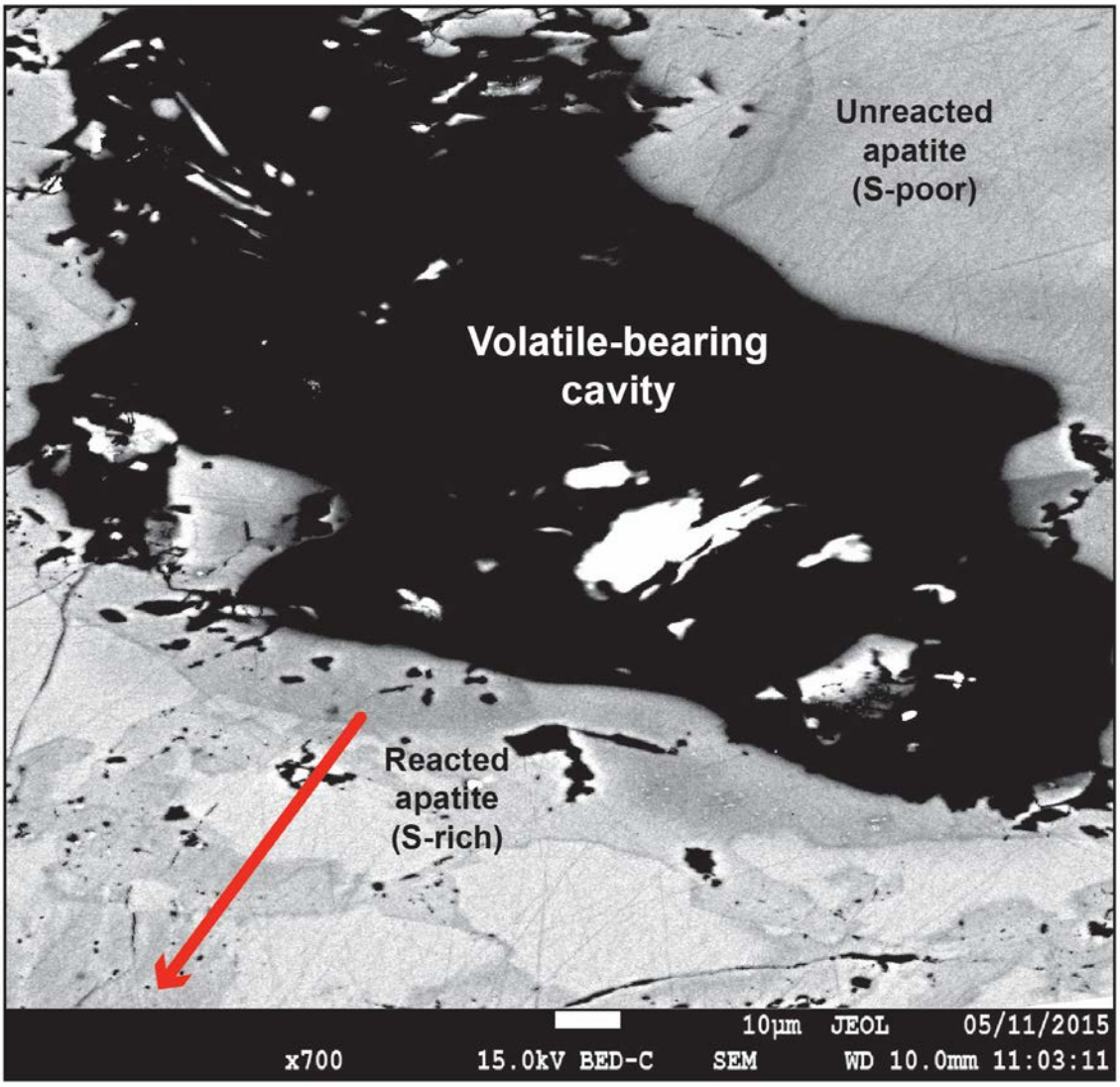

This is a preprint, the final version is subject to change, of the American Mineralogist (MSA)
Cite as Authors (Year) Title. American Mineralogist, in press.
(DOI will not work until issue is live.) DOI: http://dx.doi.org/10.2138/am-2017-5907

Figure 6A-B.

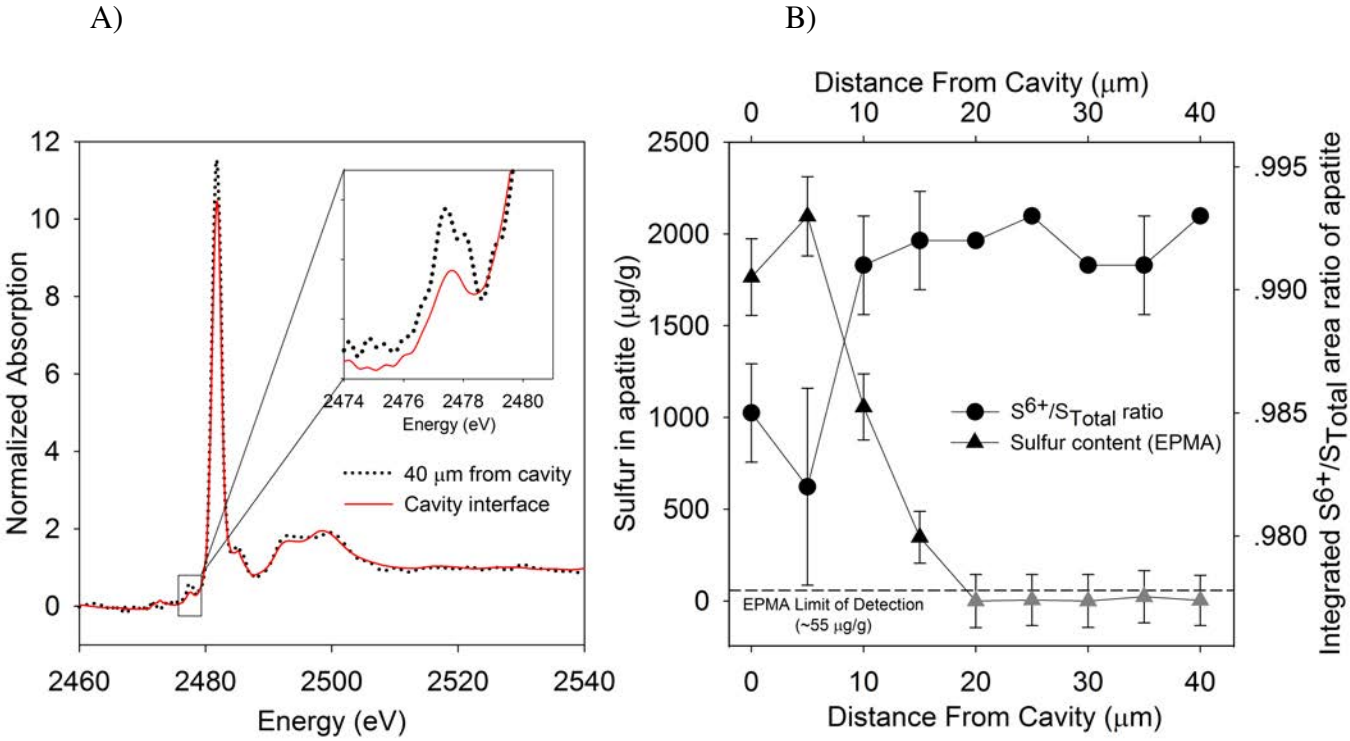

This is a preprint, the final version is subject to change, of the American Mineralogist (MSA)
Cite as Authors (Year) Title. American Mineralogist, in press.
(DOI will not work until issue is live.) DOI: http://dx.doi.org/10.2138/am-2017-5907

Figure 7A-C:

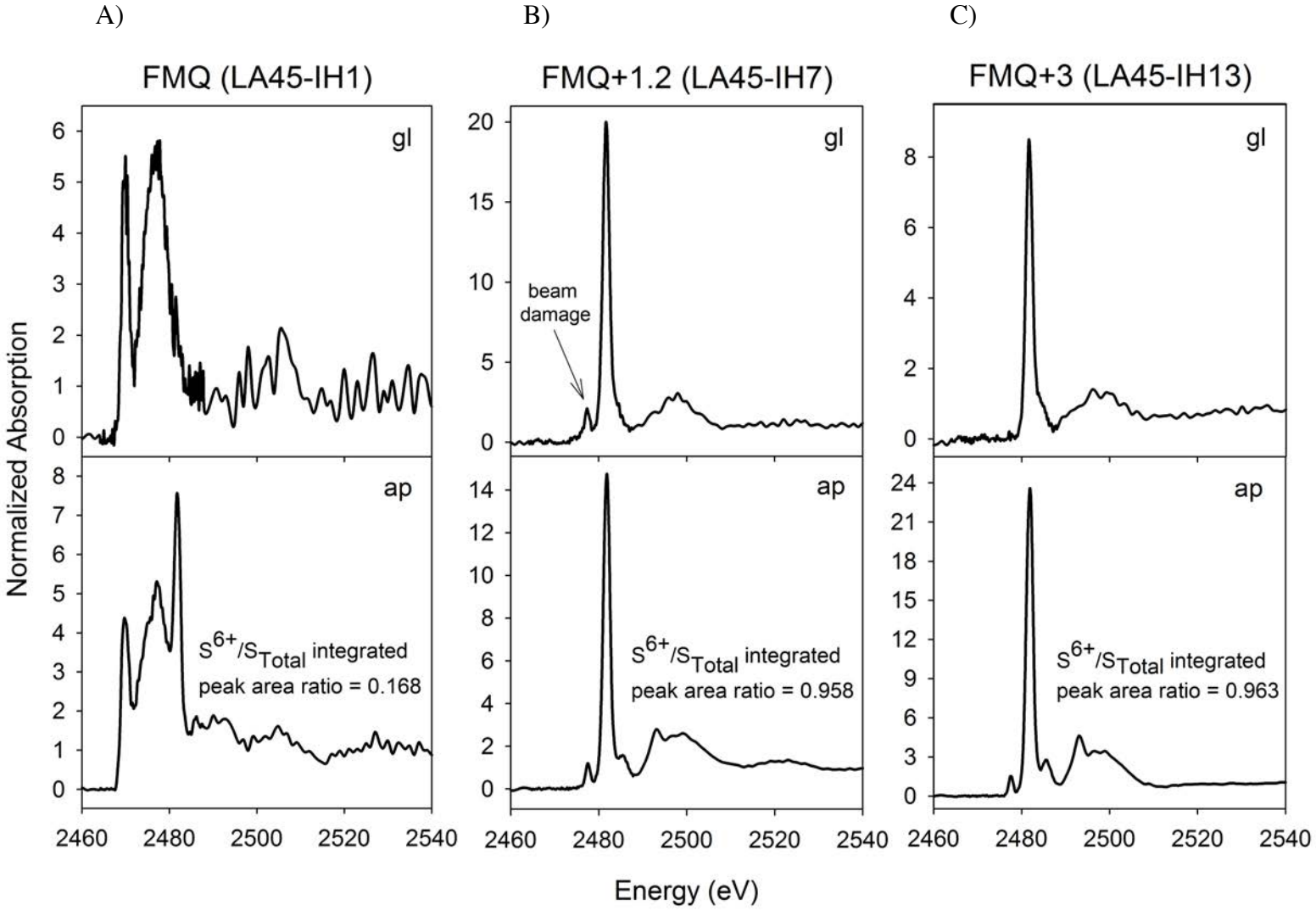

This is a preprint, the final version is subject to change, of the American Mineralogist (MSA)
Cite as Authors (Year) Title. American Mineralogist, in press.
(DOI will not work until issue is live.) DOI: http://dx.doi.org/10.2138/am-2017-5907

Figure 8A-D:

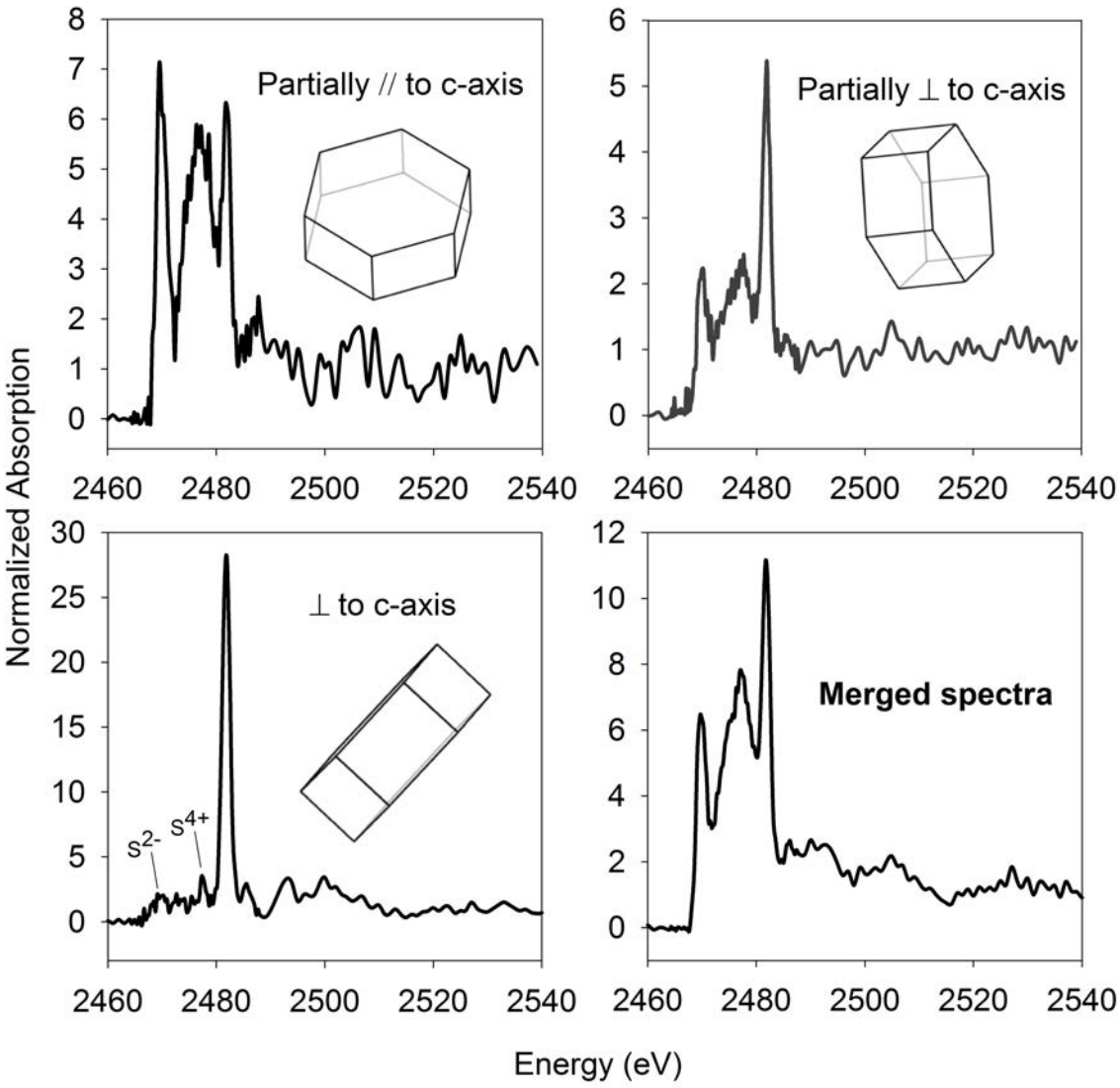

Table 1: Starting mafic (lamproite) composition

Wt.%	Lamproite AL/KB6-98*
SiO_2	40.13
TiO_2	4.37
Al_2O_3	8.57
FeO	8.75
MnO	0.20
MgO	9.21
CaO	16.24
Na_2O	0.50
K_2O	5.29
P_2O_5	3.81
H_2O	n.d.
F	n.d.
Total	97.07

Analyzed by XRF at LUH; n.d.: not determined. *Lamproite sample investigated by Luttinen et al. (2002); see their work for geological and analytical details. Loss of ignition (LOI) at 1,200^{o}C = 8.40%.

Table 2: Experimental conditions

Run name	Temperature (^{o}C)	Pressure (MPa)	fO_2 (FMQ)	Duration (days)	S added (wt. %)
LA45-IH1	1,000	300	0	3	1.0 (po.)
LA45-IH7	1,000	300	1.2	5	1.0 (po.)
LA45-IH13	1,000	300	3	5	1.0 (*po.)

*0.35 wt.% S (elemental) + 0.92 wt.% Fe_2O_3, where the Fe/S ratio corresponds to pyrrhotite (po.)

This is a preprint, the final version is subject to change, of the American Mineralogist (MSA)
Cite as Authors (Year) Title. American Mineralogist, in press.
(DOI will not work until issue is live.) DOI: http://dx.doi.org/10.2138/am-2017-5907

Supplemental Figure 1: